Microscopy and Microanalysis (2021), **27**, 758–766
doi:10.1017/S1431927621000489

Microscopy AND Microanalysis

Original Article

Quantifying Real-Time Sample Temperature Under the Gas Environment in the Transmission Electron Microscope Using a Novel MEMS Heater

Meng Li[1,2]*, De-Gang Xie[1], Xi-Xiang Zhang[3], Judith C. Yang[2] and Zhi-Wei Shan[1]*

[1]Center for Advancing Materials Performance from the Nanoscale (CAMP-Nano), State Key Laboratory for Mechanical Behavior of Materials, Xi'an Jiaotong University, Xi'an 710049, China; [2]Department of Chemical and Petroleum Engineering, University of Pittsburgh, Pittsburgh, PA 15260, USA and [3]Division of Physical Science and Engineering, King Abdullah University of Science & Technology (KAUST), Thuwal 23955-6900, Saudi Arabia

Abstract

Accurate control and measurement of real-time sample temperature are critical for the understanding and interpretation of the experimental results from *in situ* heating experiments inside environmental transmission electron microscope (ETEM). However, quantifying the real-time sample temperature remains a challenging task for commercial *in situ* TEM heating devices, especially under gas conditions. In this work, we developed a home-made micro-electrical-mechanical-system (MEMS) heater with unprecedented small temperature gradient and thermal drift, which not only enables the temperature evolution caused by gas injection to be measured in real-time but also makes the key heat dissipation path easier to model to theoretically understand and predict the temperature decrease. A new parameter termed as "gas cooling ability (H)", determined purely by the physical properties of the gas, can be used to compare and predict the gas-induced temperature decrease by different gases. Our findings can act as a reference for predicting the real temperature for *in situ* heating experiments without closed-loop temperature sensing capabilities in the gas environment, as well as all gas-related heating systems.

Key words: environmental TEM (ETEM), gas cooling effect, *in situ* heating, MEMS heater, temperature measurement

(Received 12 January 2021; revised 26 March 2021; accepted 9 May 2021)

Introduction

In situ heating experiments inside an electron microscope, such as the transmission electron microscope (TEM), have been widely used to study dynamic processes of temperature-induced structural transitions, including phase transformation, melting/sublimation (Asoro et al., 2013; Li et al., 2019), high-temperature degradation (Divitini et al., 2016; Wang et al., 2020*b*), and precipitation (Chen et al., 2006; Liu et al., 2017). In recent years, the rapid development of environmental TEM (ETEM) has brought more possibilities for *in situ* heating experiments, especially in gas–solid reaction-related fields such as catalyst reaction (Hansen et al., 2002; Hofmann et al., 2007; Simonsen et al., 2010; Behrens et al., 2012; Baldi et al., 2014; Vendelbo et al., 2014; Panciera et al., 2015; Chi et al., 2020), nanostructure growth (Sharma & Iqbal, 2004; Kodambaka et al., 2007; Hudak et al., 2014; Rackauskas et al., 2014; Panciera et al., 2015), and corrosion (Zhou et al., 2012; Zou et al., 2017, 2018; Luo et al., 2018; Curnan et al., 2019; Li et al., 2020; Wang et al., 2020*a*). Accurate control and measurement of the real sample temperature under experiment conditions are critical for the understanding and interpretation of the experimental results. However, despite developments in closed-loop temperature-controlled micro-fabricated [micro-electrical-mechanical-system (MEMS)] heaters, open-loop temperature-controlled heaters are still widely used in most commercial *in situ* TEM heating devices—including the most widely used furnace heating holders (Butler, 1979), spiral coil heating devices (Kamino et al., 2005*a*, 2005*b*; Takeo et al., 2006), and the most recent micro-fabricated (MEMS) heaters (Allard et al., 2009, 2012; Mele et al., 2016)—due to their broader availability, easier sample preparation, lower cost, and broader sample compatibility with other characterization instruments.

The open-loop temperature-controlled heaters use a heating current versus temperature curve which is precalibrated in the vacuum to infer the temperature from the applied current (Allard et al., 2009; Saka et al., 2011). For conventional TEM studies in vacuum, this method works well. But for ETEM applications, extra power will be consumed by heat convection of the injected gas, which will lead to a significant temperature drop under constant heating current/power. For example, it was reported that under 140 Pa H_2, the real sample temperature in a furnace holder dropped from 500 to only 175°C (Winterstein et al., 2015). Moreover, the real temperature is known to be affected by the experimental parameters such as gas species and gas pressure, making it unrealistic to calibrate the current–temperature curve under every condition. Consequently, a mechanistic understanding of the real temperature change under gas

*Authors for correspondence: Meng Li, E-mail: mona.mengli@gmail.com; Zhi-Wei Shan, E-mail: zwshan@mail.xjtu.edu.cn

Cite this article: Li M, Xie D-G, Zhang X-X, Yang JC, Shan Z-W (2021) Quantifying Real-Time Sample Temperature Under the Gas Environment in the Transmission Electron Microscope Using a Novel MEMS Heater. *Microsc Microanal* **27**, 758–766. doi:10.1017/S1431927621000489

conditions is essential for predicting and controlling the temperature.

Measuring real-time temperature inside TEM, especially in the gas environment, is a very challenging task. Although MEMS devices that have closed-loop temperature measurement capabilities (van Huis et al., 2009; Mele et al., 2016; van Omme et al., 2018) have emerged recently, limited by their intrinsic structure design, these commercially available MEMS devices suffer a large temperature gradient in the sample area [up to 30% from the hottest spot (Niekiel et al., 2017)]. Moreover, under the gas environment, the temperature distribution is changed, making it more difficult to investigate and model the real temperature change caused by gas. Many other methods have been also developed, including measuring the lattice spacing changes in diffraction pattern (Winterstein et al., 2015; Niekiel et al., 2017), using the gas pressure change measured from the electron energy loss spectroscopy (EELS) spectrum in closed gas cells (Vendelbo et al., 2013), using size-dependent sublimation temperature of nanoparticles to calibrate local temperature (Vijayan & Aindow, 2019), or even modifying the TEM to add a laser probe to capture local Raman spectroscopy (Picher et al., 2015). However, they usually suffer from relatively poor temperature accuracy and lack real-time temperature sensing capability during *in situ* experiments.

In this work, we report a novel home-made MEMS heating device (named as CAMP-Nano heater) that could not only accurately measure and control the real temperature under gas but also significantly improve the thermal stability of the image and the temperature uniformity. We further demonstrate how gas type, gas pressure, and the set temperature affect the sample temperature. Because of the special structure design of the CAMP-Nano heater, the key heat dissipation path by the injected gas—convection—can be modeled to predict the temperature decrease. Surprisingly, we find that a new parameter termed as “gas cooling ability (H)”, determined purely by the physical properties of the gas under ambient conditions, can be used to predict the relative temperature decrease by different gases inside ETEM.

Material and Methods

The CAMP-Nano Heater

In this work, we developed a MEMS-based *in situ* TEM heating chip that solved the aforementioned limitations of existing heaters for accurate real-time temperature control and sensing. Figure 1b illustrates the core part of the CAMP-Nano heater [for more details, see (Li et al., 2017, 2018)]. It has a specially designed free-standing hotplate that is connected to the rest of the chip only via four springs, which makes the hotplate thermally isolated from the rest of the parts of the chip, and thus leads to a very uniform temperature distribution of the hotplate that is ideal for temperature sensing shown in Figure 1c. The hotplate contains several posts for mounting samples transferred using focused ion beam (FIB). The free-standing design of the posts enables further sample thinning on the chip after FIB transfer. In addition to uniform temperature distribution, this structure also solved the long-lasting z-direction sample drift problem caused by the bulging of the heating membrane, leads to significantly improved image stability even during temperature ramping, as shown in Figure 1d. Platinum coil, which has a linear temperature coefficient of resistance and has been widely used for commercial resistance temperature detectors (RTDs) (Childs et al., 2000), was employed to heat the hotplate and sense the temperature. The resistance of the heating and sensing coil is measured via the four-terminal sensing method to ensure only the resistance on the hotplate is measured while other cable/wiring/contact resistances are counterbalanced and ruled out to make the measurement more accurate. Unlike conventional TEM heating devices that use vacuum-calibrated current–temperature curve to infer the temperature from the applied current, the hotplate temperature in our heater is calculated from the real-time measured resistance via the precalibrated temperature coefficient of resistance that is not affected by the gas condition. Hence, our heater can be used to sense the sample temperature change under gas conditions. The CAMP-Nano heater has home-made control software that can easily switch on or off the close-loop feedback control even during the heating experiment; hence, the heater could easily switch between the closed-loop control mode and the more widely used open-loop temperature control mode. When the feedback is turned off, the heating current is maintained as a constant, mimicking the open-loop heating function used in the commercial heating devices. In the open-loop mode, the temperature sensing traces on the hotplate work as temperature sensors to monitor the real-time temperature of the hotplate.

Experimental Setup

Figure 1a shows the schematic illustration of the experiment setup. A differentially pumped ETEM (Hitachi H-9500 with a home-made gas delivery system) was used to control the gas environment. Gases were injected into the specimen chamber through a needle valve, while the gas pressure of the injected gas was measured by a vacuum gauge. The CAMP-Nano heater was used to measure the temperature changing during gas injection.

The CAMP-Nano heater was first heated up to the set temperature (T_{set}) using closed-loop temperature control with feedback function turned on in the vacuum. When the temperature reaches the set temperature, the feedback function was turned off so that the heating current was maintained constant, while the temperature sensor continued to measure the real-time temperature. Gases were then let in through the needle valve to fill up the specimen chamber. The CAMP-Nano heater was located at the center of the specimen chamber, which is a few centimeters away from the gas injection needle, so the gas concentration and flow near the heating area can be considered uniform and stable.

The power of the real-time sensing capability and the feedback control function of the CAMP-Nano heater is demonstrated in Figure 1e. When feedback control is turned off, the heating current is maintained at a constant value, similar to the open-loop temperature control used in conventional TEM heating devices. Using the temperature sensor, the real-time temperature change during gas injection is detected. When hydrogen was injected with gradually increased gas pressure up to 2 Pa, the real-time temperature quickly dropped from the set temperature (T_{set} = 200°C) and then gradually leveled off to ∼176°C in a few minutes. When the gas was turned off, the temperature increased fast and then gradually back up to the set temperature, while the chamber was gradually pumped down to vacuum (base pressure of $\sim 5 \times 10^{-4}$ Pa). In comparison, when feedback control is turned on, during gas injection, the heating current quickly increased to compensate for the heat taken away by the gas, leaving the temperature constant throughout gas injection. This result demonstrates the significant impact of gas injection on the sample

https://doi.org/10.1017/S1431927621000489

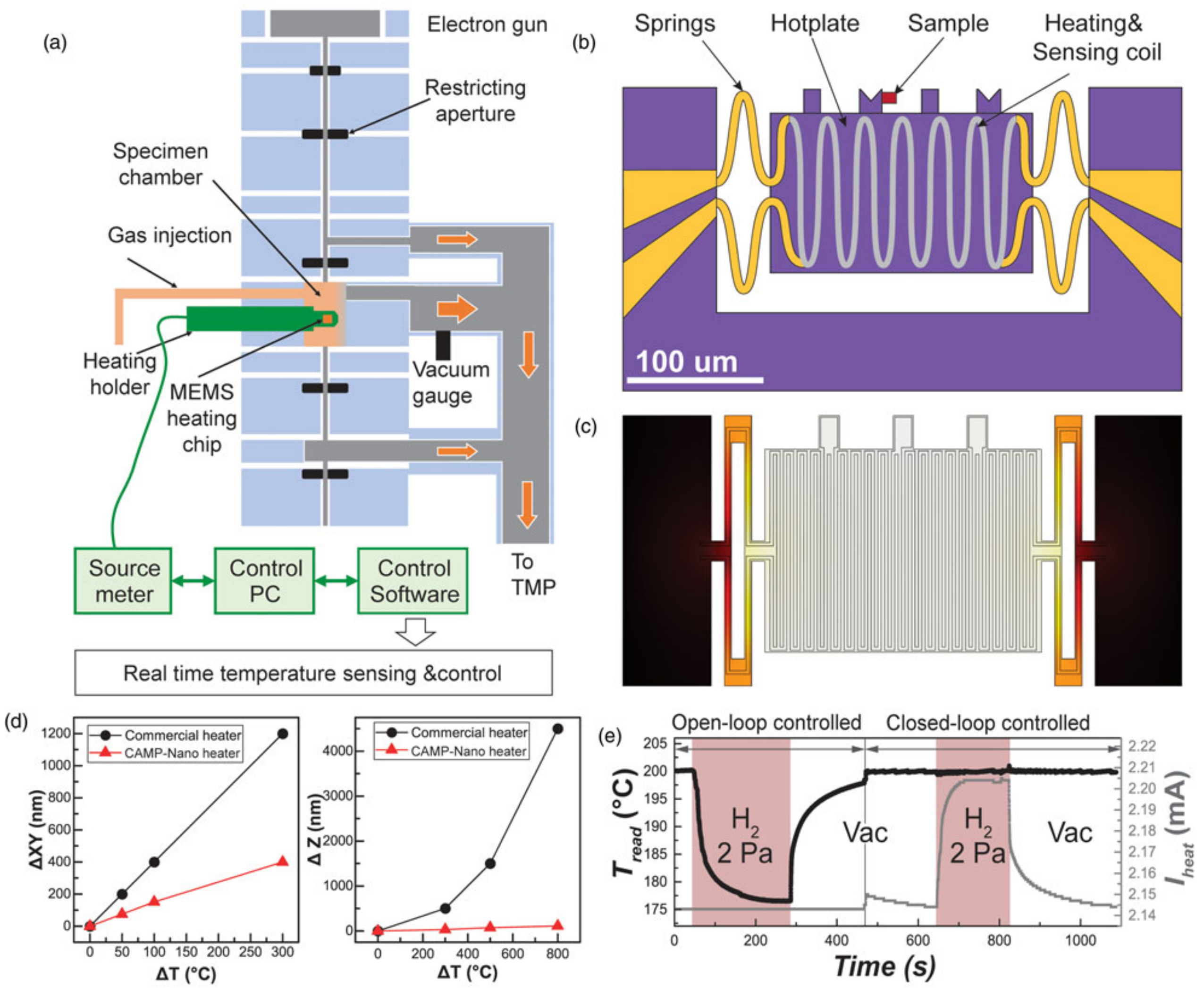

Fig. 1. Schematic illumination of the experimental setup. (**a**) Schematic of an ETEM with CAMP-Nano heater and temperature sensing system. (**b**) Schematic of the core part of the CAMP-Nano heater with real-time temperature sensing capability. (**c**) Finite element analysis (FEA) simulation shows very uniform temperature distribution on the hotplate (brighter color represents higher temperature) with ignorable temperature gradient; hence, more accurate temperature sensing and control can be achieved. (**d**) Drift distance of the CAMP-Nano heater (red triangles) in comparison with commercial heaters (black circles) under the same temperature jump measured inside the TEM. The CAMP-Nano heater shows much better image stability under temperature jump in both the planer direction (Δ*XY*) and the e-beam direction (Δ*Z*). (**e**) A typical temperature curve measured during gas injection with open-loop (left) and closed-loop (right) temperature control.

temperature and the necessity of closed-loop temperature control for gas involved heating experiments.

Measurement of Gas-Induced Temperature Change

To systematically understand the gas-induced sample temperature changes inside ETEM, controlled experiments with three variables are performed, namely set temperature (T_{set}), gas pressure (P_{gas}), and gas type. The T_{set} tested in this work is 100, 200, 300, and 400°C, respectively. The P_{gas} programmed in this work are 1, 2, 3, 4, 5 Pa for each gas species, measured by a vacuum gauge near the heating device inside the specimen chamber. The gas species explored in this work are H_2, N_2, O_2, and CO_2, all with ultra-high purity (99.999%). Each time when the injected gas pressure increased to the setpoint, the pressure was kept for more than 100 s for the gas to be uniformly distributed inside the chamber as well as for the temperature to settle. When switching gas types, the gas injection pipeline and the specimen chamber were purged several times with the aim gas and the gas concentration was confirmed by a residual gas analyzer attached to the pumping lines of the specimen chamber. To rule out the temperature contribution from the electron beam illumination (Thornburg & Wayman, 1973; Kritzinger & Ronander, 1974), the electron beam was turned off during the measurement. All temperature curves were recorded through the home-made control software.

Results and Discussion

Theoretical Analysis of the Gas-Induced Heat Dissipation Inside ETEM

Since the hotplate of the CAMP-Nano heater is thermally isolated from the rest parts, the heat dissipation of the hotplate can be simplified as a flat plate, as schematically illustrated in

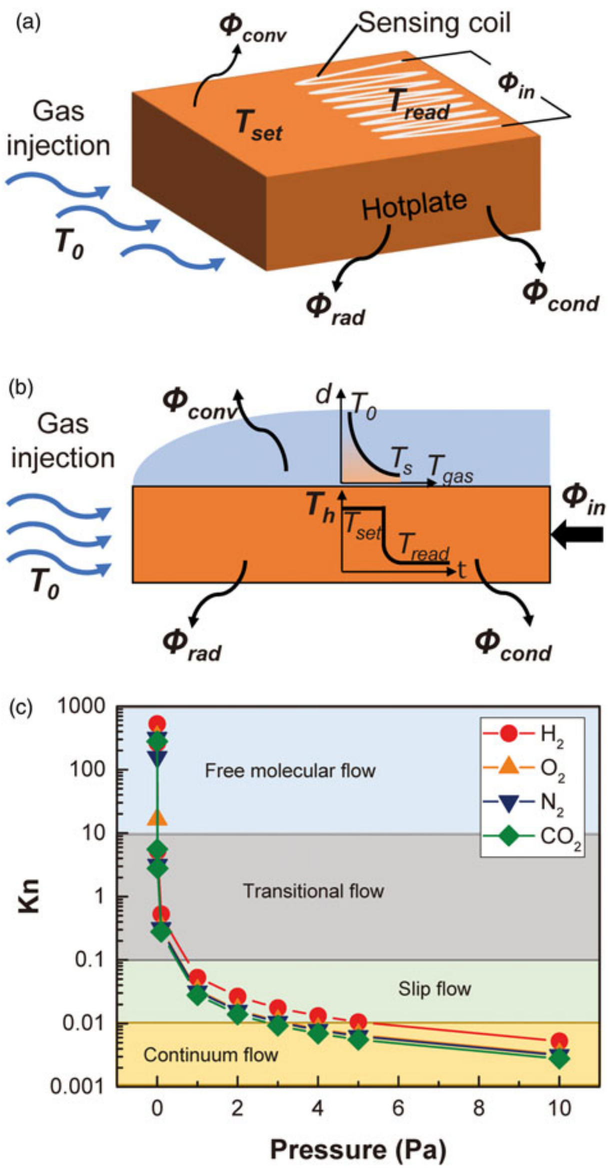

Fig. 2. Theoretical modeling of the gas effect in ETEM heating experiments. (**a**) Simplified model of the experiment setup. The hotplate area of the MEMS heater can be simplified as a flat plate. (**b**) Schematic illustration of the heat transfer model for the gas cooling effect using the heat convection on the flat plate model in classic heat transfer theory. The temperature of the gas on the surface is T_s, and the temperature of the hotplate is T_h. (**c**) Plot of the Knudsen number over gas pressure for the tested gases in ETEM.

Figure 2, which is widely used in heat transfer theories (Springer, 1971; Bergman et al., 2011; Kreith et al., 2012; Sundén & Fu, 2017*a*). The total input power Φ_{in} of the hotplate came from the Joule heating of the heating elements, hence $\Phi_{in} = I^2R$. As shown in Figure 2a, under thermal equilibrium condition with injected gas, $\Phi_{in} = \Phi_{cond} + \Phi_{rad} + \Phi_{conv}$. Where Φ_{cond} is the dissipated by heat conduction to the rest parts of the heater through the four springs, Φ_{rad} is the power consumed by thermal radiation, and Φ_{conv} is the power consumed by heat convection of the injected gas. In this work, we take Φ_{cond} and Φ_{rad} as constant for the given testing conditions and mainly consider the gas-induced temperature variation Φ_{conv} and its affecting factors.

The extra heat convection taken away by the injected gas can be simplified as the heat convection on a flat plate model illustrated in Figure 2b. After gas injection, since the input heating current remains constant, the input power is insufficient to supply the increased power consumption; hence, the hotplate temperature T_h dropped from the original set temperature T_{set} to the settled temperature under gas T_{read}. Meanwhile, the gas temperature T_g increased from ambient temperature T_0 (in this case, T_0 = room temperature) to a gradient on the hotplate surface boundary layer shown by the blue shaped area in Figure 2b, in which the gas in contact with the plate surface is heated up to T_s.

To get the function of Φ_{conv} in the flat plate heat convection model, the gas flow condition is required. Under our experiment condition ($P = 1$–5 Pa, $T_{\text{gas}} = 20$°C), the mean free path of the gas is at thousand-micrometer scale, while the dimension of the gas chamber is at ∼30 cm scale, leading to a Knudsen number (Kn) between 0.001 and 0.1, indicating a flow condition between slip flow and continuum flow (Springer, 1971; Sundén & Fu, 2017*b*). As shown in Figure 2c, for high gas pressure range (P>3 Pa for most gases), the gas flow in ETEM can be considered continuum flow; in this case, the gas temperature at the surface is the same as the heater temperature, namely $T_s = T_{\text{set}}$. While for medium gas pressure range (0.2–3 Pa), the gas flow follows slip flow; in this case, there is a temperature jump between the surface and the adjacent gas, namely $T_s = T_{\text{set}} - T_j$, where T_j is the temperature jump that depends on the gas and the surface condition (Springer, 1971; Sundén & Fu, 2017*a*). Nevertheless, the heat transfer equations for continuum flow can still be used. For lower gas pressure range, transitional flow (10^{-2}–0.1 Pa) or free molecular flow ($P < 10^{-2}$Pa) dominates, the heat transfer function is different. Moreover, for MEMS gas cells, the gas flow condition is also different due to the much smaller characteristic length for gas flow. Luckily, the gas-induced temperature change in the low gas pressure range is neglectable, and MEMS gas cells usually operate under very high pressure that obeys continuum flow and contains close-loop temperature sensing to accommodate the gas-induced temperature change. Hence, our analysis should cover most applications for gas-induced temperature change in differentially pumped ETEM.

In the continuum flow range, the gas flow speed is needed to distinguish whether the gas flow follows laminar flow or turbulence flow. In a similar experiment inside ETEM, Winterstein et al. (2015) reported a calculated Reynolds number of 0.362 under 135 Pa gas pressure, indicating laminar flow. Since the maximum gas pressure used in this work is only 5 Pa, the gas flow should also lay in the laminar flow regime. Hence, the heat convection can be calculated as (Bergman et al., 2011; Kreith et al., 2012):

$$\Phi_{\text{conv}} = \frac{\kappa A(T_s - T_0)}{L} \cdot 0.664 \cdot \sqrt[3]{\text{Pr}} \cdot \sqrt{\text{Re}}, \tag{1}$$

where Pr is the Prandtl number, Re is the Reynolds number, both numbers are determined by the gas parameters, L is the length of the hotplate, A is the surface area of the hotplate, κ is the thermal conductivity of the gas, and T_0 and T_s are the temperatures of the injected gas before and after convection shown in Figure 2b. By simplifying this equation, we can get:

$$\Phi_{\text{conv}} = 0.664 \cdot \sqrt{u} \cdot \Delta T \cdot \frac{A}{\sqrt{L}} \cdot \frac{\kappa^{2/3} \cdot c_p^{1/3} \cdot \rho^{1/2}}{\mu^{1/6}}, \tag{2}$$

https://doi.org/10.1017/S1431927621000489

where $\Delta T = T_s - T_0$ determined by the temperature difference between the hotplate and the gas, $A/\sqrt{L}$ is determined by the geometry of the hotplate, u is the flow speed of the gas determined by the gas pressure (Lafferty, 2003), while the last item of the function is determined purely by gas properties: κ—thermal conductivity, c_p—thermal capacity at constant pressure, ρ—gas density, and μ—dynamic viscosity.

In this work, we define:

$$H = \frac{\kappa^{2/3} \cdot c_p^{1/3} \cdot \rho^{1/2}}{\mu^{1/6}}. \tag{3}$$

Hence, equation (2) can be simplified as follows:

$$\Phi_{\text{conv}} \propto \sqrt{u} \cdot \Delta T \cdot \frac{A}{\sqrt{L}} \cdot H. \tag{4}$$

For slip flow, $\Delta T = T_{\text{set}} - T_0 - T_j$, where T_j is the temperature jump that depends on the gas and the surface (Springer, 1971; Sundén & Fu, 2017*b*):

$$T_j = \frac{2-\alpha}{\alpha}\frac{2\gamma}{\gamma+1}\cdot\frac{\lambda}{\text{Pr}}\cdot\frac{\partial T_g}{\partial d}\ , \tag{5}$$

where α is the gas accommodation coefficient that depends on the gas type and surface material and condition, and λ is the mean free path of the gas that depends on gas type, pressure, and temperature.

Based on equation (4), the key factors that affect gas-induced heat dissipation inside ETEM can be summarized as follows:

1) Gas pressure effect: the larger gas flow speed u, the higher gas pressure P_{gas}. Therefore, higher gas pressure is expected to cause a larger temperature drop for given testing conditions.
2) Set temperature effect: the larger ΔT between the gas and hotplate, the more power will be consumed by heat convection Φ_{conv}; hence, a larger temperature drop is expected. Given fixed T_0, as used in our experiment, a higher T_{set} means a larger temperature drop.
3) Heater geometry effect: the larger the heating area A, the more power consumption by heat convection Φ_{conv} and larger temperature drop will be expected. Because the surface area of a traditional furnace heater is usually ~100 times larger than a MEMS heater, the temperature drop for a conventional furnace heater is expected to be much larger than the MEMS heaters for given testing conditions.
4) Gas species effect: Gases with larger H will cause more temperature drop.

Next, we will demonstrate that equation (4) is at least quantitatively correct to predict the gas-induced temperature evolution.

Effect of Gas Pressure and Set Temperature

Figure 3a shows a typical measured temperature curve with stepwise increased H_2 gas pressure. The hotplate was heated to a set temperature T_{set} of 400°C in the vacuum, then the feedback control function was turned off in the home-made control software to maintain a constant heating current. At ~60 s, H_2 gas was injected with a stepwise profile up to 5 Pa with steps of 1 Pa and the gas pressure was kept constant for ~60 s at each step. As can be seen in the plot, the temperature readout changes simultaneously with the pressure change and is quite stable at each constant step period. When the gas was turned off at ~300 s, the temperature returns to the initial set temperature together with the pumping down of the chamber vacuum. Obviously, higher pressure led to a larger temperature drop, as predicted by equation (4).

To better compare the temperature drop at different set temperatures, we define another parameter— the normalized temperature T_N —as follows:

$$T_N = \frac{T_{\text{read}} - T_0}{T_{\text{set}} - T_0}, \tag{6}$$

where T_{read} represents real-time temperature. T_N can be understood as the ratio of the temperature difference between heater and gas [ΔT in equation (4)] after and before gas injection. For example, when $T_{\text{set}} = 400$°C, the real temperature dropped to 333.9°C under 5 Pa H_2, so the normalized temperature T_N = 82.6%, indicating the relative temperature difference between the heater and the gas after gas injection is 82.6% of the value before gas injection.

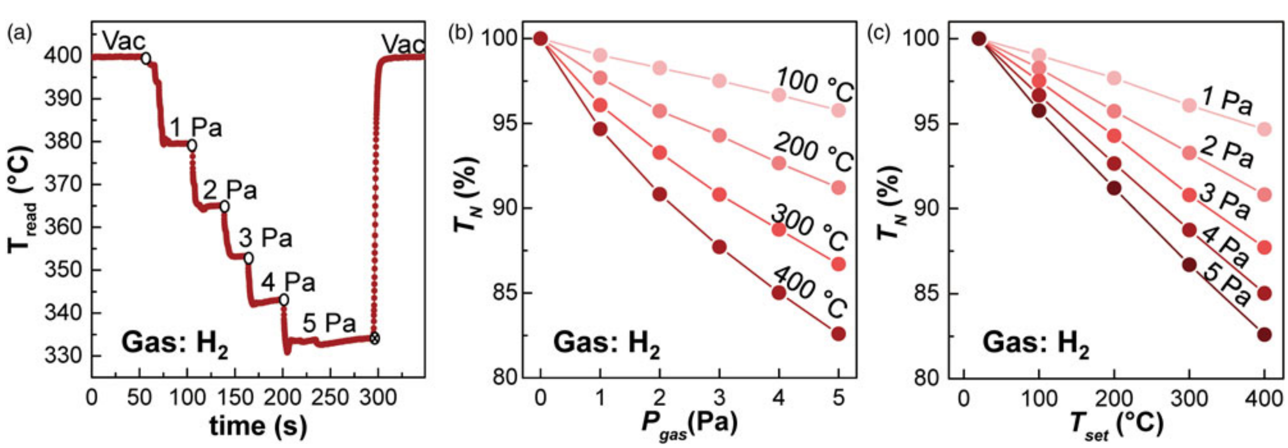

Fig. 3. Effects of gas pressure and set temperature under H_2 gas flow. (**a**) The real temperature (T_{read}) decreases with increasing H_2 gas pressure P_{gas}. (**b**) Normalized temperature (T_N) decreases linearly with increasing gas pressure P_{gas} under various initial temperatures T_{set}. (**c**) Normalized temperature (T_N) decreases linearly with set temperature T_{set} under different gas pressure.

https://doi.org/10.1017/S1431927621000489

Using this normalized temperature, the temperature drop with increasing gas pressure under different set temperature can be directly compared, as plotted in Figure 3b. Each curve shows the evolution of the normalized temperature in response to the pressure increase under the same set temperature. As shown in Figure 3b, for a given set temperature, the normalized temperature decreases with increasing gas pressure. The higher the set temperature, the larger the normalized temperature drop. Again, the observed phenomena agree well with equation (4).

It is worth noting that curves shown in Figure 3b are gradually deviating from linear fitting along with the increase of the set temperature. This can be rationalized as below: the power consumed by heat convection Φ_{conv} is proportional to the square root of the gas flow speed u, $\Phi_{conv} \propto \sqrt{u}$. The steady-state gas flow speed is determined by the gas pressure and ETEM pumping speed, which increases with increasing gas pressure and gradually decrease the increase rate until a maximum speed is reached (Lafferty, 2003). So, the gas flow speed is expected to increase with increasing gas pressure, and the speed will gradually approach a constant value determined by the maximum pumping speed of the ETEM. Hence, the normalized temperature is expected to decrease nonlinearly with increasing gas pressure.

Similarly, the effect of set temperature under given gas pressures is plotted in Figure 3c, and each curve shows the normalized temperature change in response to increasing set temperature. Under the same gas pressure, the higher the set temperature, the larger the normalized temperature drop. The T_N decreases linearly with increasing set temperature, which meets the prediction by equation (4). Using equation (6), the read temperature decreases parabolically with increasing set temperature.

Effect of Heater Geometry

Although only the CAMP-Nano heater was used in this work, the prediction on the heating area can be verified by other literature reports. Winterstein et al. (2015) measured the temperature change of the furnace heater and MEMS heater using the lattice parameter change in the diffraction pattern of Ag nanoparticles, and found under 140 Pa H_2, the temperature of furnace heater dropped from 500 to ∼175°C, while the MEMS heater only dropped from 400 to ∼220°C.

Effect of Gas Species

We found that under a given set temperature and pressure, different gases can cause very different temperature drop, as summarized in Figure 4. Four different gases were tested in our work, including H_2, N_2, O_2, and CO_2. As plotted in Figure 4a, under the same set temperature T_{set} = 400°C, the normalized temperature drops with increasing gas pressure P_{gas} for all tested gases, and the relative decrease amount ranks in the order of $H_2 > O_2 \approx N_2 > CO_2$ at every tested gas pressure. Similarly, as plotted in Figure 4b, under the same gas pressure P_{gas} = 5 Pa, the normalized temperature also drops linearly with increasing set temperature T_{set}, and the relative decrease amount ranks in the same order of $H_2 > O_2 \approx N_2 > CO_2$ at every tested set temperature. When T_{set} = 400°C, P_{gas} = 5 Pa, the normalized temperature drop ΔT_N caused by H_2, O_2, N_2, and CO_2 are 17.4, 7.9, 7.9, and 6.2% respectively, namely the real temperature drops by 66.1, 29.9, 29.8, and 23.4°C respectively.

To know the relative cooling ability of different gases in a more intuitive manner, we define relative normalized temperature drop $\Delta T_{RN} = \Delta T_{N,\mathrm{gas}}/\Delta T_{N,\mathrm{H_2}}$. As shown in Figure 5a, for T_{set} = 400°C, the ΔT_{RN} versus gas species curves are similar to each other with the ΔT_{RN} increasing with increasing gas pressure for the same gas. The difference in the absolute value for each gas might stem from the justification of the slip flow of the gas under lower pressure. While for P_{gas} = 5 Pa, as shown in Figure 5b, the ΔT_{RN} almost remains unchanged for each gas for the T_{set} ranged from 100 to 400°C. This inspired us to consider that the relative cooling ability is a more physical properties-dependent parameter and, therefore, should be linked with H, as we defined in equation (3). Using the physical properties of the gases shown in Table 1, the value of H for different gases can be calculated. Similarly, we define relative gas cooling ability $H_R = H_{\mathrm{gas}}/H_{\mathrm{H_2}}$. Surprisingly, the trend of H_R versus gas species is very similar to that of ΔT_{RN}, as shown in Figure 5c. It is worth noting that all the parameters listed in Table 1 are measured under ambient temperature and pressure, that is 20°C and 1 atm, the values might change under different temperature and pressure, which might be the reason for the deviation between the calculated value in Figure 5c and experimental value in Figures 5a and 5b. Nevertheless, the relative ratio among different gases meets well with the experimental results. Therefore, it can be concluded that H can be used as a scale to

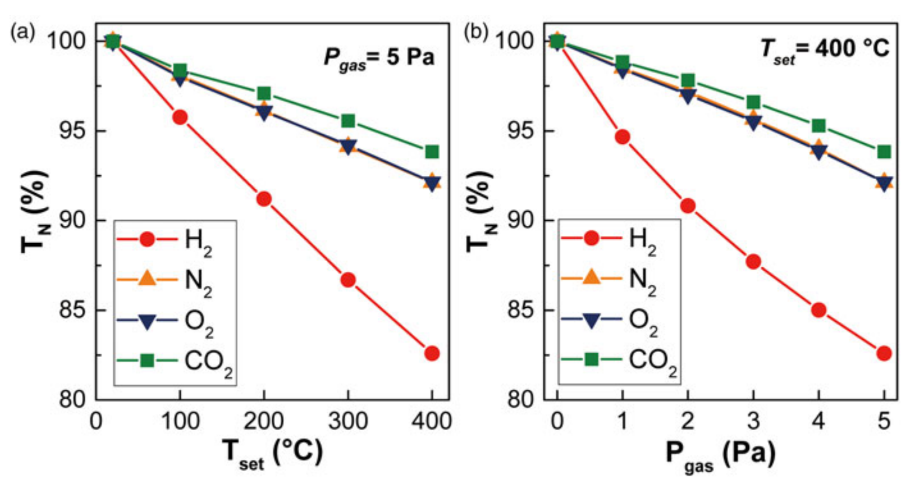

Fig. 4. Effect of gas species. (**a**) Evolution of T_N versus P_{gas} under T_{set} = 400°C for four different gases. (**b**) Evolution of T_N versus T_{set} under P_{gas} = 5 Pa for four different gases.

https://doi.org/10.1017/S1431927621000489

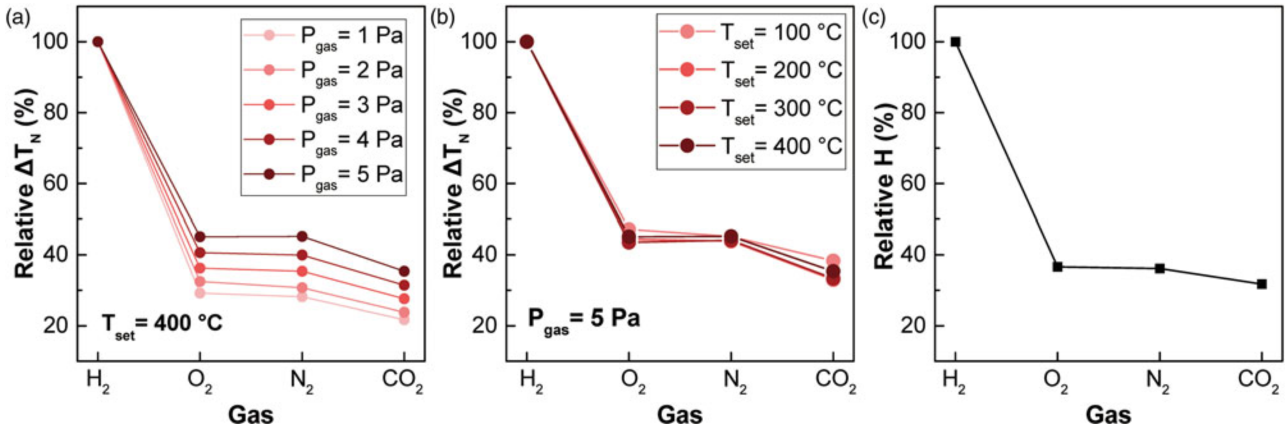

Fig. 5. The relationship between relative normalized temperature drop ($\Delta T_{RN} = \Delta T_{N,\mathrm{gas}}/\Delta T_{N,\mathrm{H_2}}$) and the relative gas cooling ability ($H_R = H_{\mathrm{gas}}/H_{\mathrm{H_2}}$). (**a**) ΔT_{RN} versus gas species with P_{gas} = 1–5 Pa and T_{set} = 400°C. (**b**) ΔT_{RN} versus gas species with T_{set} = 100–400°C and P_{gas} = 5 Pa. (**c**) H_R versus gas species under ambient temperature and pressure.

Table 1. Physical Properties of Some Typical Gas Species and Their Calculated Cooling Abilities.

Gas Species	Density (ρ)[a] kg/m^3	Heat Capacity ($C_{p,m}$)[a] J/(gK)	Thermal Conductivity (k)[a] W/(mK)	Dynamic Viscosity (μ)[a] $\times 10^{-6}$ Ns/m^2	Cooling Ability (H)	Relative Cooling Ability (H_R) %
H_2	0.0899	14.32	0.168	8.8	0.1024	**100**
He	0.1664	5.19	0.142	19.6	0.0777	**75.9**
Air	1.205	1.01	0.0262	18.2	0.0398	**38.8**
O_2	1.331	0.919	0.024	20.4	0.0375	**36.6**
N_2	1.165	1.04	0.024	18.9	0.0370	**36.1**
CO	1.165	1.02	0.0232	17.4	0.0364	**35.6**
CO_2	1.842	0.844	0.0146	14.7	0.0325	**31.7**
Ar	1.661	0.52	0.016	22.3	0.0260	**25.4**

[a]Parameters measured at 20°C and 1 atm. The bold values are calculated values of H_R for the plot in Figure 5.

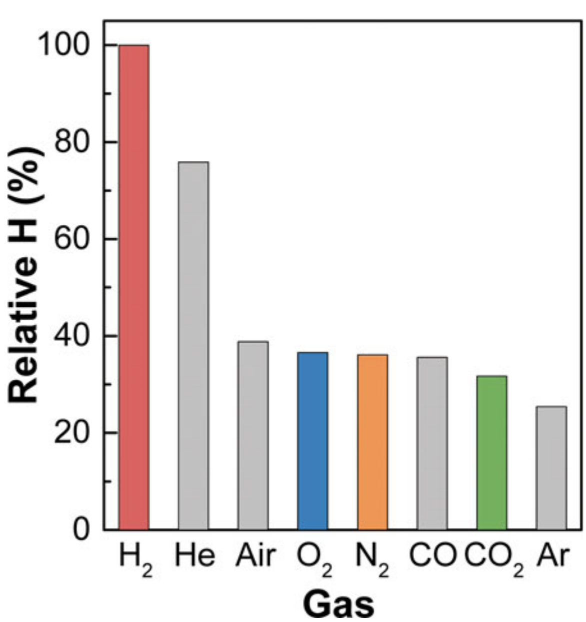

Fig. 6. Predicting the gas cooling effect of typical gas species used in ETEM by calculated relative cooling ability (H_R). The predicted gas cooling effect follows the trend of H_2 > He > Air > $O_2 \approx N_2 \approx$ CO > CO_2 > Ar.

reflect the cooling ability among different gases, regardless of pressure and temperature. Consequently, we term H as the gas cooling ability. Our findings were further supported by the following facts: by calculating the H of commonly used gas species as listed in Table 1 and plot them all together in Figure 6, the following gas cooling trend can be inferred: H_2> He > Air > $O_2 \approx N_2 \approx$ CO > CO_2 > Ar. This meets well with previous literature reports that H_2 and He cause the most significant temperature decrease (Picher et al., 2015).

Conclusion

In summary, in this work, a novel home-made MEMS heating device with a thermally isolated hotplate and real-time temperature sensing capability was developed, which enables accurate real-time temperature measurement and simplifies the theoretical modeling to quantify the gas effect on the sample temperature during *in situ* heating experiments in ETEM. Our theoretical modeling deduced the equation to calculate the power consumed by the injected gas to predict the temperature change. A new parameter, gas cooling ability H, which is determined purely by some physical parameters of the gas, is defined to predict the temperature decrease under different gas species. Our results show that the real temperature of the heating devices is very sensitive to the gas environment, for example, even 5 Pa of H_2 can cause the temperature to drop from 400 to 333°C. Hence, for *in situ* heating experiments under the gas environment, real-time temperature sensing and closed-loop temperature control are essential for accurate temperature. However, open-loop heating devices are still widely used. For open-loop heating devices, the real temperature under gas needs to be compensated. The temperature drop caused by gas injection is determined by gas type, gas pressure, heater temperature T_{set}, and heating area A of the heating device. Our results indicate that the normalized temperature drop ΔT_N increases nonlinearly with increasing gas pressure P_{gas} and linearly with increasing initial heater temperature T_{set}. And among the tested gas species, the gases follow the order of $H_2 > O_2 \approx N_2 > CO_2$. Using the calculated H, the temperature drop caused by different gases can be predicted in the order of $H_2 >$ He > Air > $O_2 \approx N_2 \approx CO > CO_2 >$ Ar. These results can act as a reference to predict the real temperature of *in situ* TEM heating experiments in the gas environment to better understand and explain the experimental observations. These results would also be helpful for all gas-related heating systems.

Acknowledgments. We acknowledge Dr. Longqing Chen, Ms. Chunxiu Tian, and Dr. Qiang Zhang from KAUST for the help in MEMS design and fabrication, Ms. Bo Fu from Xi'an Jiaotong University (XJTU) for the helpful discussions in the theory part, and Ms. Qinqin Fu from XJTU and Hitachi High Technologies for the technical supports.

Financial support. This work is supported by the National Key Research and Development Program of China (No. 2017YFB0702001) and National Natural Science Foundation of China (grant numbers NSFC 5203000210, 51621063), National Science Foundation (grant numbers NSF DMR-1508417, CMMI-1905647), and the International Joint Laboratory for Micro/Nano Manufacturing and Measurement Technologies. The MEMS fabrications were performed at King Abdullah University of Science and Technology (KAUST).

References

Allard LF, Bigelow WC, Jose-Yacaman M, Nackashi DP, Damiano J & Mick SE (2009). A new MEMS-based system for ultra-high-resolution imaging at elevated temperatures. *Microsc Res Tech* **72**(3), 208–215.

Allard LF, Overbury SH, Bigelow WC, Katz MB, Nackashi DP & Damiano J (2012). Novel MEMS-based gas-cell/heating specimen holder provides advanced imaging capabilities for *in situ* reaction studies. *Microsc Microanal* **18**(4), 656–666.

Asoro MA, Kovar D & Ferreira PJ (2013). *In situ* transmission electron microscopy observations of sublimation in silver nanoparticles. *ACS Nano* **7**(9), 7844–7852.

Baldi A, Narayan TC, Koh AL & Dionne JA (2014). *In situ* detection of hydrogen-induced phase transitions in individual palladium nanocrystals. *Nat Mater* **13**(12), 1143–1148.

Behrens M, Studt F, Kasatkin I, Kuhl S, Havecker M, Abild-Pedersen F, Zander S, Girgsdies F, Kurr P, Kniep BL, Tovar M, Fischer RW, Norskov JK & Schlogl R (2012). The active site of methanol synthesis over Cu/ZnO/Al_2O_3 industrial catalysts. *Science* **336**(6083), 893–897.

Bergman TL, Incropera FP, DeWitt DP & Lavine AS (2011). *Fundamentals of Heat and Mass Transfer*. United Kingdom: John Wiley & Sons.

Butler EP (1979). *In situ* experiments in the transmission electron microscope. *Rep Prog Phys* **42**(5), 833–895.

Chen JH, Costan E, van Huis MA, Xu Q & Zandbergen HW (2006). Atomic pillar-based nanoprecipitates strengthen AlMgSi alloys. *Science* **312**(5772), 416–419.

Chi H, Curnan MT, Li M, Andolina CM, Saidi WA, Veser G & Yang JC (2020). *In situ* environmental TEM observation of two-stage shrinking of Cu_2O islands on Cu(100) during methanol reduction. *Phys Chem Chem Phys* **22**(5), 2738–2742.

Childs PRN, Greenwood JR & Long CA (2000). Review of temperature measurement. *Rev Sci Instrum* **71**(8), 2959–2978.

Curnan MT, Andolina CM, Li M, Zhu Q, Chi H, Saidi WA & Yang JC (2019). Connecting oxide nucleation and growth to oxygen diffusion energetics on stepped Cu(011) surfaces: An experimental and theoretical study. *J Phys Chem C* **123**(1), 452–463.

Divitini G, Cacovich S, Matteocci F, Cinà L, Di Carlo A & Ducati C (2016). In situ observation of heat-induced degradation of perovskite solar cells. *Nat Energy* **1**, 2.

Hansen PL, Wagner JB, Helveg S, Rostrup-Nielsen JR, Clausen BS & Topsoe H (2002). Atom-resolved imaging of dynamic shape changes in supported copper nanocrystals. *Science* **295**(5562), 2053–2055.

Hofmann S, Sharma R, Ducati C, Du G, Mattevi C, Cepek C, Cantoro M, Pisana S, Parvez A, Cervantes-Sodi F, Ferrari AC, Dunin-Borkowski R, Lizzit S, Petaccia L, Goldoni A & Robertson J (2007). *In situ* observations of catalyst dynamics during surface-bound carbon nanotube nucleation. *Nano Lett* **7**(3), 602–608.

Hudak BM, Chang YJ, Yu L, Li G, Edwards DN & Guiton BS (2014). Real-time observation of the solid-liquid-vapor dissolution of individual tin(IV) oxide nanowires. *ACS Nano* **8**(6), 5441–5448.

Kamino T, Yaguchi T, Konno M, Watabe A, Marukawa T, Mima T, Kuroda K, Saka H, Arai S, Makino H, Suzuki Y & Kishita K (2005*a*). Development of a gas injection/specimen heating holder for use with transmission electron microscope. *J Electron Microsc* **54**(6), 497–503.

Kamino T, Yaguchi T, Sato T & Hashimoto T (2005*b*). Development of a technique for high resolution electron microscopic observation of nanomaterials at elevated temperatures. *J Electron Microsc* **54**(6), 505–508.

Kodambaka S, Tersoff J, Reuter MC & Ross FM (2007). Germanium nanowire growth below the eutectic temperature. *Science* **316**(5825), 729–732.

Kreith F, Manglik RM & Bohn MS (2012). *Principles of Heat Transfer*. United States: Cengage Learning.

Kritzinger S & Ronander E (1974). Local beam heating in metallic electron microscope specimens. *J Microsc* **102**(2), 117–124.

Lafferty JM (2003). Vacuum technology. In *Encyclopedia of Physical Science and Technology(Third Edition)*, Meyers, R. A. (Ed.), pp. 385–410. New York: Academic Press.

Li J, Wang Z, Li Y & Deepak FL (2019). *In situ* atomic-scale observation of kinetic pathways of sublimation in silver nanoparticles. *Adv Sci* **6**, 8.

Li M, Curnan MT, Gresh-Sill MA, House SD, Saidi WA & Yang JC (2021). Unusual layer-by-layer growth of epitaxial oxide islands during Cu oxidation. *Nature Communications* **12**(1), 2781. doi:10.1038/s41467-021-23043-w.

Li M, Xie DG, Ma E, Li J, Zhang XX & Shan ZW (2017). Effect of hydrogen on the integrity of aluminium-oxide interface at elevated temperatures. *Nat Commun* **8**, 14564.

Li M, Xie D-G & Shan Z-W (2018). Development of a novel bulk sample TEM heater and its application. *Microsc Microanal* **24**(S1), 1830–1831.

Liu C, Malladi SK, Xu Q, Chen J, Tichelaar FD, Zhuge X & Zandbergen HW (2017). *In-situ* STEM imaging of growth and phase change of individual CuAlX precipitates in Al alloy. *Sci Rep* **7**(1), 2184.

Luo L, Su M, Yan P, Zou L, Schreiber DK, Baer DR, Zhu Z, Zhou G, Wang Y, Bruemmer SM, Xu Z & Wang C (2018). Atomic origins of water-vapour-promoted alloy oxidation. *Nat Mater* **17**(6), 514–518.

Mele L, Konings S, Dona P, Evertz F, Mitterbauer C, Faber P, Schampers R & Jinschek JR (2016). A MEMS-based heating holder for the direct imaging of simultaneous *in-situ* heating and biasing experiments in scanning/transmission electron microscopes. *Microsc Res Tech* **79**(4), 239–250.

Niekiel F, Kraschewski SM, Muller J, Butz B & Spiecker E (2017). Local temperature measurement in TEM by parallel beam electron diffraction. *Ultramicroscopy* **176**, 161–169.

Panciera F, Chou YC, Reuter MC, Zakharov D, Stach EA, Hofmann S & Ross FM (2015). Synthesis of nanostructures in nanowires using sequential catalyst reactions. *Nat Mater* **14**(8), 820–825.

Picher M, Mazzucco S, Blankenship S & Sharma R (2015). Vibrational and optical spectroscopies integrated with environmental transmission electron microscopy. *Ultramicroscopy* **150**, 10–15.

Rackauskas S, Jiang H, Wagner JB, Shandakov SD, Hansen TW, Kauppinen EI & Nasibulin AG (2014). *In situ* study of noncatalytic metal oxide nanowire growth. *Nano Lett* **14**(10), 5810–5813.

https://doi.org/10.1017/S1431927621000489

Saka H, Kamino T, Ara S & Sasaki K (2011). *In situ* heating transmission electron microscopy. *MRS Bull* **33**(2), 93–100.

Sharma R & Iqbal Z (2004). *In situ* observations of carbon nanotube formation using environmental transmission electron microscopy. *Appl Phys Lett* **84**(6), 990–992.

Simonsen SB, Chorkendorff I, Dahl S, Skoglundh M, Sehested J & Helveg S (2010). Direct observations of oxygen-induced platinum nanoparticle ripening studied by *in situ* TEM. *J Am Chem Soc* **132**(23), 7968–7975.

Springer GS (1971). Heat transfer in rarefied gases. *Adv Heat Transfer* **7**, 163–218.

Sundén B & Fu J (2017*a*). Aerodynamic heating. In *Heat Transfer in Aerospace Applications*, pp. 27–44.

Sundén B & Fu J (2017*b*). Low-density heat transfer. *In Heat Transfer in Aerospace Applications*, pp. 45–70. Elsevier.

Takeo K, Toshie Y, Mitsuru K, Akira W & Yasuhira N (2006). Development of a specimen heating holder with an evaporator and gas injector and its application for catalyst. *J Electron Microsc* **55**(5), 245–252.

Thornburg D & Wayman C (1973). Specimen temperature increases during transmission electron microscopy. *Phys Status Solidi (A)* **15**(2), 449–453.

van Huis MA, Young NP, Pandraud G, Creemer JF, Vanmaekelbergh D, Kirkland AI & Zandbergen HW (2009). Atomic imaging of phase transitions and morphology transformations in nanocrystals. *Adv Mater* **21**(48), 4992–4995.

van Omme JT, Zakhozheva M, Spruit RG, Sholkina M & Pérez Garza HH (2018). Advanced microheater for *in situ* transmission electron microscopy; enabling unexplored analytical studies and extreme spatial stability. *Ultramicroscopy* **192**, 14–20.

Vendelbo SB, Elkjaer CF, Falsig H, Puspitasari I, Dona P, Mele L, Morana B, Nelissen BJ, van Rijn R, Creemer JF, Kooyman PJ & Helveg S (2014). Visualization of oscillatory behaviour of Pt nanoparticles catalysing CO oxidation. *Nat Mater* **13**(9), 884–890.

Vendelbo SB, Kooyman PJ, Creemer JF, Morana B, Mele L, Dona P, Nelissen BJ & Helveg S (2013). Method for local temperature measurement in a nanoreactor for *in situ* high-resolution electron microscopy. *Ultramicroscopy* **133**, 72–79.

Vijayan S & Aindow M (2019). Temperature calibration of TEM specimen heating holders by isothermal sublimation of silver nanocubes. *Ultramicroscopy* **196**, 142–153.

Wang Y, Li M, Yang Y, Zhao Xa, Ma E & Shan Z (2020*a*). *In-situ* surface transformation of magnesium to protect against oxidation at elevated temperatures. *J Mater Sci Technol* **44**, 48–53.

Wang Z, Tang Y, Zhang L, Li M, Shan Z & Huang J (2020*b*). *In situ* TEM observations of discharging/charging of solid-state lithium-sulfur batteries at high temperatures. *Small* **16**(28), 1–8.

Winterstein JP, Lin PA & Sharma R (2015). Temperature calibration for *in situ* environmental transmission electron microscopy experiments. *Microsc Microanal* **21**(6), 1622–1628.

Zhou G, Luo L, Li L, Ciston J, Stach EA & Yang JC (2012). Step-edge-induced oxide growth during the oxidation of Cu surfaces. *Phys Rev Lett* **109**(23), 235502.

Zou L, Li J, Zakharov D, Stach EA & Zhou G (2017). *In situ* atomic-scale imaging of the metal/oxide interfacial transformation. *Nat Commun* **8**(1), 307.

Zou L, Yang C, Lei Y, Zakharov D, Wiezorek JMK, Su D, Yin Q, Li J, Liu Z, Stach EA, Yang JC, Qi L, Wang G & Zhou G (2018). Dislocation nucleation facilitated by atomic segregation. *Nat Mater* **17**(1), 56–63.